Measuring strain caused by ion implantation in GaN

Pedro José de Sousa Mendes

pedro.s.mendes@tecnico.ulisboa.pt

Abstract

Gallium nitride (GaN), whose applications in technology were responsible for the award of the 2014 Nobel Prize in Physics, is one of the most important groundwork materials for the new generation of optoelectronic devices. To study its reaction to ion implantation (doping) fourteen samples, seven grown along a-plane (non-polar) and another seven along c-plane (polar), on a sapphire substrate were implanted with 300 keV Argon (Ar) ions, at room temperature (RT). The implanted fluences ranged from 5×10^{12} atoms/cm^2 to 8×10^{15} atoms/cm^2. The subsequent structural analysis was performed using two techniques, Rutherford Backscattering/Channeling (RBS/C) and high-resolution X-Ray Diffraction (XRD). The results allow not only further speculation on the existing hypothesis that perpendicular strain caused by implantation may be the driving force behind defect transformation processes inside the lattice, but also seem to confirm a lower Relative Defect Level (RDL) for a-GaN implanted with 8×10^{15} at/cm^2, in comparison with c-GaN for the same implantation fluence, as reported previously. Even if not conclusive, these are promising results as the research on the applications of non-polar nitrides in LEDs and lasers, which, in comparison to polar nitrides, avoid polarization phenomena, is constantly developing.

Keywords: *Gallium Nitride, Implantation, Backscattering, Channeling, X-Ray Diffraction, Strain*.

1. Introduction and objectives

Gallium nitride (GaN), discovered in 1932 is a chemical compound which belongs to the family of the III-nitride compounds (gallium, the cation, is an element in the group 3 of the periodic table and has an abundance on Earth of 13 ppm). Gallium nitride and associated semiconductor devices are among the most important optoelectronics breakthroughs of the last decades. Ever since the development of Shuji Nakamura's first GaN-based light-emitting diodes (LEDs) [1] in the early 90s, which would later win 2014 Nobel Prize in Physics *"for the invention of efficient blue light-emitting diodes, which has enabled bright and energy-saving white light sources"*, nitride-based semiconductors became worldwide known. GaN-based violet lasers are the groundwork of the Blu-Ray system, one of the examples of new generation's optical data storage processes [2]. This format made it possible to increase the information storage capacity of an optical disc from 4.7 Gb to 54 Gb. High-Electron Mobility Transistors (HEMTs) and Field-Effect Transistors (FETs) are other technologically relevant examples of the applications of GaN electronics [3].

Semiconductors are characterized by the possibility of modulating their conducting properties by an intentional and controlled introduction of external elements into their crystalline structure. Three key material properties are fundamental to host ion implantation doping for optical application: damage resistance, thermal stability and wide direct bandgap [4], and these are all characteristics of GaN and related materials, making them excellent candidates. Ion implantation allows both controlling the local dopant distribution and introducing more than one dopant while the solubility limits can possibly be overcome. However, this technique also presents an important disadvantage as it creates structural defects in the crystal lattice, which highly diminishes the optical performance.

One of the most efficient techniques to study implantation damages is the Transmission Electronic Microscopy (TEM), which provides the possibility of determining the nature of implantation defects by a direct observation of these; for this reason, while this technique has not been used to perform this work, references to the work of several groups on TEM will be frequent. Other techniques include Rutherford Backscattering Spectrometry/Channeling (RBS/C) – to determine the dependence of defects with depth – and X-Ray Diffraction (XRD), which provides an overview of the strain caused by the creation of structural defects as well as techniques probing the optical and electric properties of the materials. While c-GaN implantation has been widely studied [5]–[11], there are considerably fewer articles regarding a-GaN – which has been pointed out as being more resistant and presenting distinct extended defects [12], [13]. It is proposed that strain caused by implantation defects is one of the driving forces for the formation of extended defects [11], [14], so by measuring it both damage and annealing processes can be better comprehended.

The goal of this Master's dissertation is to study and compare the argon-implantation damage formation in gallium nitride grown following the a-plane orientation and the c-plane orientation (usually referred henceforward as a-GaN and c-GaN). This will continue the work presented in [12] using a combination of

RBS/C and TEM, with the improvement of using the XRD technique to complement this data and analyze an implantation process in similar conditions and to compare those results with the published literature. We aim to understand the strain caused by ion implantation because it is believed that it is the cause of the atoms' motion in the lattice leading to defect transformation [11] and this has not been studied in a-GaN yet.

The choice of implanting Argon relies on the fact that it is an inert element. Therefore, and while its implantation is used for fundamental research only, it plays a key role in understanding how other dopants behave – structural defects are the same regardless of the implanted atom –, thus contributing to a better understanding of the potential applications of ion implantation for the fabrication of GaN-based electronics.

While the sample growth process took place in the group of Prof. Scholz at the Institute of Optoelectronics, University of Ulm, Germany, all the subsequent phases of this project, from the implantation of the samples to the experimental techniques and data analysis was performed at LATR (Laboratory of Accelerators and Radiation Technologies) at Campus Tecnológico e Nuclear, Instituto Superior Técnico, Lisbon.

2. State of the art

Gallium nitride structural properties

III-nitrides present two common crystal structures, zinc-blende and wurtzite, being the latter the most stable structure for GaN. The basic unit of this structure is a hexagonal primitive cell with two parameters, "c" and "a". c-planes are polar planes as they contain either only gallium or nitrogen atoms, while a-planes present the same number of each element: by imagining a replication of the crystalline structure presented in Figure 1, four Ga^{3+} ions are shared at the corner between six hexagonal cells each ($4/6\times3^{+}$ charges) and two N^{3-} ions are shared between three hexagonal cells each ($2/3\times3^{-}$ charges), thus are non-polar planes [15].

Figure 1 presents a schematic of GaN crystalline wurtzite structure, including the crystallographic planes relevant for this work.

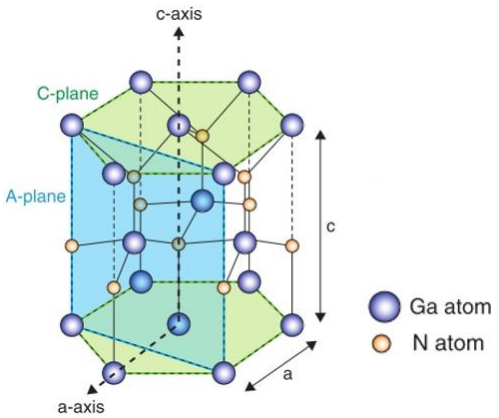

Figure 1 – Wurtzite crystal structure of GaN. Adapted from [16]. The lattice parameters are a=3.189 Å and b=5.185 Å.

The wurtzite structure has two interpenetrating hexagonal sublattices, where every atom of each element is surrounded by four of the other element. Its lattice constants given in Figure 1 are the typically reported values in the literature for relaxed crystals [17], however, these parameters can be influenced by the free-electron concentration [18]. It is usual to identify the various planes on a wurtzite structure by using the so-called Miller (also called Miller-Bravais) indexes *hkil*, where $-i = h + k$ is defined to better understand the similarity of the planes parallel to the c-axis. Figure 2 illustrates the definition of the Miller indexes and the sketch of c- and a-planes. The four indexes [*hkil*] are related to the three unitary vectors **a**, **b**, **d** and **c**, respectively. According to the Miller indexes system, the c-orientation is defined as <0001> and the a-orientation comes as <11$\bar{2}$0> by permutation of the indexes [19]. Each GaN wurtzite lattice contains two c-planes and six a-planes, where c-planes are perpendicular to a-planes.

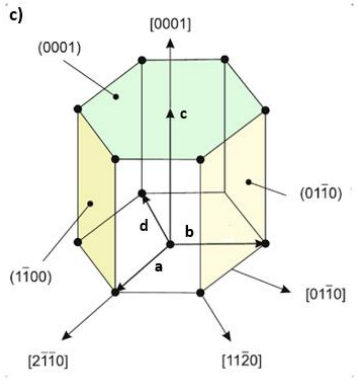

Figure 2 - Definition of the Miller indexes for the wurtzite structure. Adapted from [19], [20].

The energy required in GaN to promote an electron from the valence band to the conduction band, thus originating a current flow, is of 3.4 eV [16], making this material a wide bandgap semiconductor – it is also defined as direct bandgap because the crystal momentum of holes and electrons is the same in both bands. This value corresponds to an emission wavelength of 365 nm. GaN is considered as a very good thermal conductor, a quantity that has been shown to decrease with the doping density [21]. This characteristic makes applications of GaN in optoelectronics and high-power/high-temperature very promising.

As mentioned before, GaN films are usually grown on sapphire substrates [22], whose lattice constants are different between both materials thus creating a so-called lattice mismatch of 14-16% [18], [23]. Even with the introduction of AlN and SiN_x buffer layers [22], [24]–[26] to reduce this mismatch, it cannot be entirely eliminated. Adding up to the different thermal expansion coefficients between film and substrate, tensions will inevitably be created on the grown films. It has been shown that piezoelectric and spontaneous polarizations are present in GaN films grown on the c-plane (polar), attributed to the macroscopic polarization between III-V nitrides heterojunctions [27]. This phenomenon affects the optoelectronic properties of devices such as LEDs and lasers, so the research on

the growth of non-polar films [15] is becoming popular in the past years as they have been shown to overcome this problem [28].

Ion implantation in GaN

Ion beam processing of materials results from the introduction of atoms into the surface layer of a solid substrate by bombardment of the material with ions within the electron-volt to mega-electron-volt energy range. Optical, mechanical, electrical, magnetic and superconducting properties are all affected (or even dominated) by the presence of the implanted atoms. Using energetic ions allows introducing a wide variety of atomic species independently of thermodynamic factors – making it conceivable to obtain impurity concentrations and distributions of interest which otherwise would not be attainable. These benefits have been stimulated by the opportunities of synthesizing novel materials with eventual applications in the tribological, corrosion, semiconductor and optical fields. Ion beam processing provides an alternative and non-equilibrium technique of introducing dopant atoms into a matrix [4].

The first implantation study in c-plane GaN took place in 1974 [5] when Pankove and Hutchby studied its photoluminescence following Zn implantation. Nearly 20 years ago, Tan *et al.* [6] observed that low fluence implantation, followed by 1100 °C annealing, created a wide defect network, while for high fluences it could lead to amorphization. Kalinina *et al*. presented a study of Mg implanted GaN p-n junctions [7]. Kucheyev *et al*. reviewed early studies on the ion-beam processing of GaN in 2001 [8]. The same Australia-based group typically combined RBS/C and TEM techniques to study ion bombardment in $Al_xGa_{1-x}N$ films [29]. All these studies were performed on thin films grown following the c-plane orientation. The effects of ion implantation are characterized by strong dynamic annealing [8], [30], i.e. point defects created during the implantation are very mobile and can either recombine or gather to form extended defects such as stacking faults and dislocation loops during the implantation process [10], [23]. The diffusion and formation/annealing of defects has been widely studied [8], [30], [31].

Strain

The study of strain in GaN and related materials has been going on since the end of last century, as ion bombardment has been shown to induce large hydrostatic strains and expand GaN lattice parameters [9], [31]–[34]. This study is usually performed with the X-Ray Diffraction technique, which allows, among a big range of possibilities, the determination of the lattice parameters of the material, providing information on the perpendicular induced strain.

Several groups have been developed models to describe the evolution of strain profiles inside crystalline lattices [34], [35], which have then turned into simulation codes [34], [36], [37]. This is justified by the recent proposal for the strain to be one of the driving forces of defect transformation [11], [14]. Regarding the comparison of strain between a-plane and c-plane orientations, Catarino *et al*. [13] showed an expansion of the *a* parameter when implanting a-GaN and the *c* parameter when implanting c-GaN, thus, an expansion of the perpendicular parameter – with respect to the surface, for each planar orientation – following implantation damage. Recently, a mechanism to explain the development of strain in irradiated materials was proposed, considering the transformation of clusters of point defects into extended defects which will, first, induce elastic strain, and second, merge into a net of dislocation lines, allowing strain relaxation [38].

Previous work

The most recent work of our group [12] presented an overview of the differences between the implantation effects in GaN thin films grown along different crystallographic directions. 300 keV Argon ions at 15 K with fluences ranging between 2×10^{12} and 4×10^{16} atoms/cm^2 were implanted in a-, c- and m-plane surface oriented epitaxial GaN layers. Similar fluence values have been implanted at 300 K for the elaboration of this Master's thesis, as it has been observed that thermal effects on damage formation mechanisms in GaN appear to be of small importance [11], [39]. Three steps of damage build-up were identified, correlating the Relative Defect Level (RDL) taken from RBS/C analysis with the implanted fluence, a behavior which has been studied previously [11], [14], [30], [39]. Regarding XRD, it has been recently shown that it loses sensitivity for c-GaN at high implantation fluences by our group. Faye *et al*. [33], following a 200 keV Argon implantation at room temperature (RT), showed a first strain saturation at around 0.5%, occurring for fluences ranging from 1×10^{15} at/cm^2 to 2×10^{16} at/cm^2, and a second strain saturation at around 1.8%. Furthermore, we detected that strain saturation occurred at a lower fluence in comparison to the RDL saturation threshold, thus indicating an insensitivity of the XRD technique at high fluences. It was suggested a change in the microstructure to explain this strain saturation [33].

3. Experimental techniques

Sample growth and ion implantation

Our wafers were kindly provided by Prof. Scholz, Institute of Optoelectronics, University of Ulm, and grown via MOVPE – Metal Organic Vapor Phase Epitaxy. In MOVPE, precursor elements – in our case, ammonia (NH_3), trimethylgallium (TMGa) and trimethylaluminum (TMAl) – are transported by a carrier gas (in this case, Pd-diffused H_2) to the substrate, where these precursors will take part in several chemical reactions at the surface. Both a-plane and c-plane GaN samples had sapphire (Al_2O_3) starting substrates [40], respectively, r-oriented and c-oriented. Regarding c-plane samples, the film is about 2.75 µm thick [25], while a-plane samples are 5.2 µm thick [41]. AlN and SiN intermediate layers were also deposited, the first to compensate the lattice mismatch and the second to reduce the dislocation density.

Argon was implanted at room temperature, with an energy of 300 keV and a 7º incident angle between the beam and the sample normal to minimize channeling effects. It is possible to simulate its profile with Monte Carlo simulations by using the code SRIM – the Stopping and Range of Ions in Matter [42]. The maximum range of Argon ions was reached at 380 nm, a value that is crucial to understand the results presented in this work. The projected range for Ar is at a depth of 190 nm, while the higher number of vacancies is predicted to occur at around 130 nm depth. The implantation of Argon in GaN was performed at the LATR, Campus Tecnológico e Nuclear. The chosen implanted fluences were, for seven samples grown on each planar orientation, 5×10^{12} at/cm^2, 5×10^{13} at/cm^2, 2×10^{13} at/cm^2, 5×10^{14} at/cm^2, 1×10^{15} at/cm^2, 2×10^{15} at/cm^2 and 8×10^{15} at/cm^2. These values correspond to the regimes I, II and III took from the work of Lorenz *et al*. [12] at 15 K and the reason for not having implanted fluences higher than 8×10^{15} at/cm^2 is due to the XRD low-sensitivity for higher fluences, shown by Faye *et al*. [33] and explained previously.

Rutherford Backscattering/Channeling (RBS/C)

To study the concentration of defects in both a-plane and c-plane GaN samples and determine the implantation defect profile with depth, the RBS/C technique plays an important role [43]. This technique is based on Geiger and Marsden's experiment in 1909, who observed the backscattering of alpha particles when these collided with the nuclei of gold atoms – the very same reason why Rutherford would suggest a new atomic model two years later. Combining with ion channeling, it allows us to determine the implantation defect profile (with 10-30 nm depth resolution). RBS is used to study superficial layers of solid materials. When a monoenergetic He^+ ions beam enters a solid, part of these ions is backscattered already at the surface. Most of these ions penetrate the material and lose energy by electronic excitation, due to a large amount of the collisions with the electrons.

RBS is the most used ion beam technique, being one of its major advantages the possibility of combining it with channeling and allowing the study of defects as well as the lattice site location of dopants inside crystalline structures. If the incident beam is aligned with a major crystal direction of the single crystal, it is guided through small angle interactions and via the electrical potential (Coulomb) created by the atoms' nuclei which align to create the channels. This channeling is crucially dependent on the incident angle, which must be similar than the critical angle Ψ.

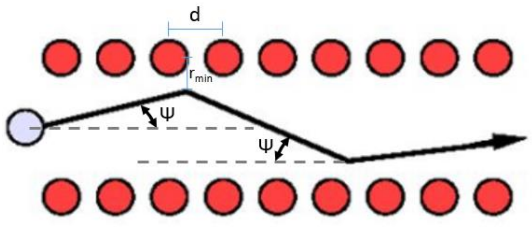

Figure 3 - Trajectory of the channeling of a particle.

We can define the minimum yield for a hypothetical perfect crystal as [44]:

$$\chi_{min} = \frac{\pi r_{min}^2}{nd}, \quad (1)$$

where the numerator indicates the impact area around the atomic line and the denominator are calculated by multiplying the atomic density *n* by the distance between the atoms *d* (Figure 3), giving the superficial area of the atomic line – if a particle hits one of these lines, it will be backscattered.

To perform our analysis, the energy of the He^+ ion beam is of 2000 keV and the detector angle is of 140º. RBS was performed under the same conditions for both a-GaN and c-GaN samples, being the incident angle for the random spectrum of 5º. The aligned spectra were obtained with an incident angle of approximately 0º, a value for which the backscattering was observed to be the smallest. As we first optimize the channeling of the beam through the crystalline structure, the higher the value of the backscattering yield – the more ions the beam finds that will make it be backscattered and detected -, the more damaged the implanted sample.

As mentioned previously, the ion channeling technique is very useful to characterize the defect profile inside a crystalline structure. To extract the damage profile from the RBS/C spectra, it is essential to determine the variation of the minimum yield for a real crystal as a function of the depth. In Equation 2, Y is the yield, in every channel, from each spectrum (implanted or as-grown, aligned or random) [45]:

$$\Delta\chi_{min} = \frac{Y_{alig}^{impl} - Y_{alig}^{as-grown}}{Y_{random}}. \quad (2)$$

The relative damage level (RDL), which correlates the relative concentration of displaced lattice atoms versus depth, was determined by using a code that implements a two-beam model [46] in order to account for the dechanneling background. Dechanneling happens when the concentration of defects inside the sample is too high for the beam to keep on being channeled inside the lattice.

X-Ray Diffraction (XRD)

The discovery of the x-rays is usually attributed to Wilhelm Röntgen, the first Nobel Prize in Physics winner of the XX century. It could, however, be mentioned that this finding and subsequently the Nobel Prize could have been awarded to Nikola Tesla instead [47]. He had been independently doing research on the topic since 1894 and it is thought to have captured an x-ray image few weeks before Röntgen's statement of the discovery in late December of 1895. The reasons why Tesla never claimed credit for being the first to identify this new radiation are not only because the discoveries were made too close in time, but also since most of his research was lost in a fire that burnt down his laboratory in New York in March of 1895. Both scientists mutually congratulated and respected each other's work.

Around 20 years later, Bragg realized that, although the scattering process is very complex, the reflection of x-rays can be mathematically treated like any other

reflection – in the sense that the reflected angle is equal to the incident angle. Bragg's Law (or condition) comes as:

$$n\lambda = 2dsen(\theta), \quad (3)$$

where *d* stands for the distance between atomic plans, *θ* is the incident angle and λ is the wavelength of the x-rays. The position of the diffracted beam is described by the angle 2θ with respect to the incident beam. It is possible to define the distance *d* as a function of Miller indices *h, k, l*, becoming d_{hkl}. The XRD geometry considered for our measurements were symmetric reflections, where we are measuring atomic planes parallel to the surface.

Given the fact that it is sensitive to small variations of the lattice parameters, the XRD technique is a very efficient technique to measure the strain caused by implantation defects inside the crystalline structure. The perpendicular strain, $\varepsilon^{\perp}$, is defined as:

$$\varepsilon^{\perp} \equiv \frac{\Delta x}{x_0} = \frac{x - x_0}{x_0}, \quad (4)$$

where x_0 represents the lattice parameter of the as-grown sample (*a*- or *c*-GaN) and x stands for the expanded lattice parameter, whose expansion is determined by the 2θ angle [33].

The XRD diffractograms where simulated with RaDMaX – Radiation Damage in Materials analysed with X-ray diffraction –, an open-source code developed in Limoges, France, used to determine strain and damage depth profiles in implanted crystalline materials [36]. This is a software which was developed to study implantation induced strain and extract strain and damage profiles. It allows fitting experimental 2θ-ω XRD data, combining fitting algorithms and providing as input perpendicular strain and static Debye-Waller (DW) factor.

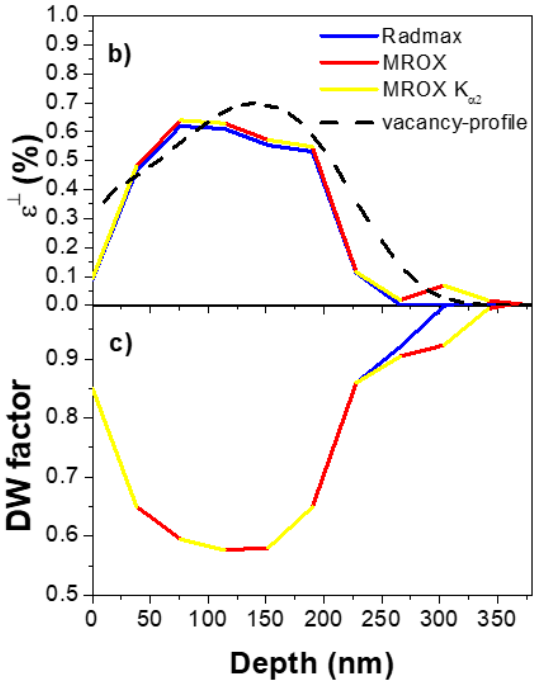

Figure 4 – Strain and DW factor profiles of an a-plane sample with an implanted fluence of 5 × 10^{13} atoms/cm^2. Ten layers with the same thickness were defined, with a pre-defined Gaussian-like shape for strain profile (in red) and its "mirror" for DW. The damage depth is 380 nm, from SRIM.

RaDMaX was, initially, compared to MROX – Multiple Reflection Optimization package for X-ray diffraction –, a code developed by Doctor Sérgio Magalhães which, in opposition to RaDMaX, allows not only defining two consecutive layers with the same deformation and different thicknesses to different layers but also simulating the effect of residual $K_{\alpha 2}$ radiation in our diffractograms and the presence of layers of other materials in the film [34]. Figure 4 shows an example of the functionalities of MROX, considering the $K_{\alpha 2}$ line effect, from the X-Ray Cu source.

As a conclusion, MROX not only gives the same solution as RaDMaX for the same conditions, but its versatility allows the possibility of simulating effects that were seen to appear in our diffractograms. However, factors such as the temporal limitation for the elaboration of this work and the simplicity of the usage of RaDMaX were considered and ultimately led to the choice of this software for the presentation of the simulated results of the XRD measurements performed for this work.

4. Results

RBS/C results

The as-grown samples for both planar orientations exhibit very good crystal qualities, with minimum yield values around 2% for a-GaN and 2.6% for c-GaN – which corresponds to usual values measured for state-of-the-art epitaxial GaN films [48]. The aligned RBS/C spectra present a high backscattering yield even for unimplanted regions (below channel ~460), which are due to the dechanneling of the He^+ beam and suggest the existence of extended defects [12].

To extract and quantify the defect profiles, the relative defect level (RDL) as a function of depth was extracted as described previously, which allows a more quantitative analysis of the results. Figure 5 presents three different stages of damage accumulation and their profiles, where the RDL corresponds to the fraction of displaced atoms.

The first row shows an increase of the defect level with fluence; its shape corresponds well to SRIM simulations for vacancy profiles, for both planar orientations. It is then possible to identify a saturation of the defect level for both planar orientations on the second row, regime II (although at a slightly higher RDL is observed for a-GaN). On the third row, the shape of the profile clearly deviates from SRIM simulations for both materials, an occurrence which has been reported previously [49]. For c-GaN, the damage close to the surface is much lower than expected – suggesting a recombination of defects, as reported previously [11], [39], proposed to occur at higher temperatures by Wendler *et al*. For a-GaN, the depth of maximum damage changes considerably and it is found at the depth of maximum Ar-concentration. For fluences below 8 × 10^{15} at/cm^2, none presents an RDL higher than 0.035 for the c-plane orientation, while it occurs for a-plane oriented samples; this difference can, however, be attributed to the associated error to these measurements.

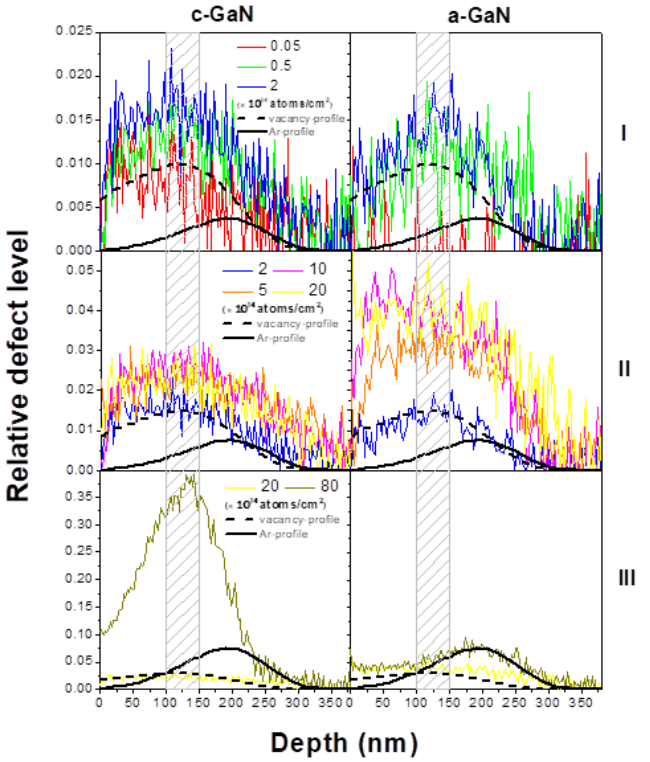

Figure 5 - Relative defect level profiles derived from the RBS/C spectra using a two-beam model for both planar orientations. Numbers on the right side of each row indicate the three different damage build-up stages. The distributions of argon and vacancies simulated using the code SRIM are included for comparison, with arbitrary units. The area between 100 and 150 nm is highlighted as it corresponds to the depth window used to plot the damage build-up (Figure 6).

It is difficult to identify substantial differences between planar orientations for the fluences of the first stage, and both present almost the same relative defect level for all the three second stage fluences – even if for a-GaN their values are slightly higher than the ones for c-GaN.

Figure 6 represents the average RDL in a depth window from 100 nm to 150 nm (indicated in Figure 5 as the highlighted gray area) as a function of the fluence. This region corresponds to the value where the SRIM vacancy-profile reaches its maximum. The error bar is the error associated with the calculation of the difference in the minimum yield for the 100-150 nm window between the implanted and as-grown sample, $\Delta\chi_{min}$, by recovering Equation 2.

Error bars are the result of the error propagation for Equation 2, by stating the error in the yield, ΔY, as 10%. Figure 6 also shows the damage accumulation curve obtained in [12] by fitting the experimental data using the Hecking model of implantation damage build-up [50]. The Hecking model data showed in this figure corresponds to the implantation and measurements done at 15 K and was included only for comparison.

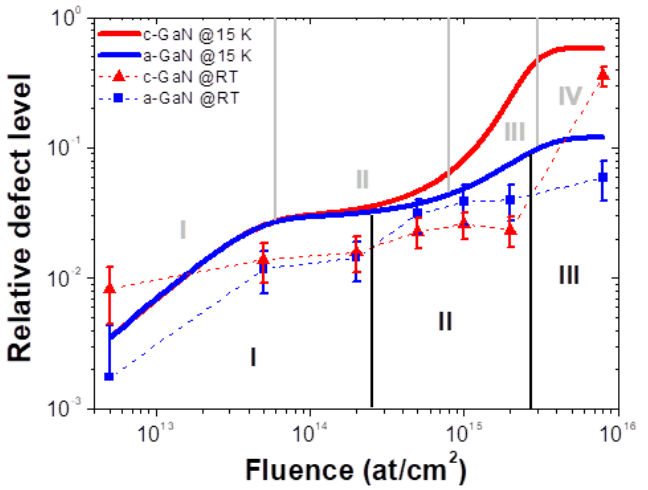

Figure 6 - Damage build-up curves. Simulated curves using Hecking's model from Lorenz et al. [12] at 15 K are shown for comparison with measured points (symbols and dashed lines) for both a-GaN and c-GaN.

Therefore, while our fluence range corresponds to four stages at 15 K and taking into consideration the associated error, our measured points seem to correspond to only the first three regimes, as it has been shown for c-GaN by Pagowska *et al.* [14]: for low fluences (from 5×10^{12} to 2×10^{14} at/cm^2), the RDL slowly increases with the fluence (first regime). On the second regime (from 5×10^{14} to 2×10^{15} at/cm^2), the RDL saturates, while the third regime (for the 8×10^{15} at/cm^2 fluence) indicates a steep increase of the RDL for c-GaN and a much smaller variation for a-GaN. The higher radiation resistance for this regime for a-GaN has been reported previously both for Ar-implantation (at 15 K) [12] and for Eu-implantation (at room temperature) [13].

XRD results

To study the induced strain in both planar orientations, XRD analysis was performed for all implanted fluences, measuring 2θ-ω scans of symmetric reflections. In terms of Miller indexes (*hkil*) the symmetric reflection measured for c-GaN is the 0002 and for a-GaN is the $11\bar{2}0$. Figure 7 presents the 2θ-ω scans for both crystal orientations. It shows that, after implantation, implanted volume peaks are formed for lower 2θ angles (higher *c* and *a* lattice parameters for c-GaN and a-GaN, respectively) with respect to the main Bragg peak. For both planar orientations, up to a fluence of 2×10^{15} at/cm^2, the implanted volume peaks are well-defined and suggest that homogeneously strained layers are formed. By increasing the fluence, it is possible to identify an increased perpendicular lattice strain, given by a shift on the implanted volume peak to lower 2θ angles. For the highest fluence (8×10^{15} at/cm^2), the position of its implanted volume peak does not change compared to the previous fluence (at around $\varepsilon^{\perp} = 0.65\%$ and $\varepsilon^{\perp} = 0.9\%$ for c-GaN and a-GaN, respectively) and the implanted volume peak broadens strongly. The bad definition of the peak for this fluence is given to the fact that the sample is already strongly damaged.

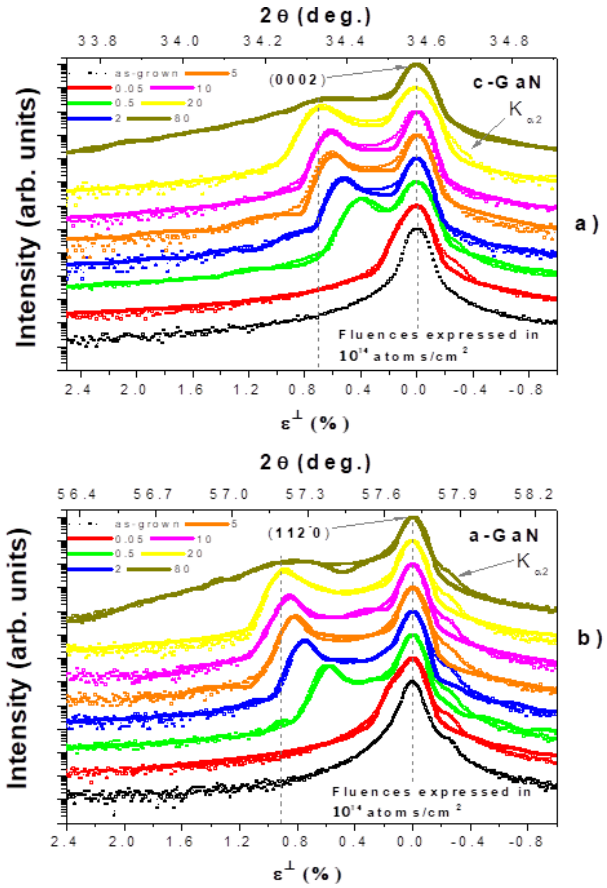

Figure 7 - XRD diffractograms (symbols) around the (0002) reflection for c-GaN (a) and (11$\bar{2}$0) reflection for a-GaN (b), implanted to different fluences. For the lower x-axis, the 2θ angle was converted to perpendicular strain. The low-intensity peaks at the high angle side of the main peak (more evident for a-GaN) are attributed to instrumental artifacts due to an incomplete filtering of the $K_{\alpha 2}$ Cu X-Ray line by the monochromator. Fluences are expressed in 10^{14} atoms/cm^2. Lines indicate RaDMaX simulated fits and as it is easier to distinguish lines from dots, the legend is given in function of the lines.

The same pattern was already observed for c-GaN implanted with Ar at 200 keV where strain saturation occurs for higher fluences [33]. In fact, at these high fluences, the XRD technique becomes insensitive to further defect formation which is why the fluences in the present thesis were restricted to the low fluence regimes.

The diffractograms were then simulated with RaDMaX software to accomplish a better understanding of the strain and the crystalline quality of the material (given by the static Debye-Waller, DW, factor). These fittings were obtained by adjusting the strain and DW factor input values. Implantation defects are known to induce large hydrostatic strain, leading to the dilatation of the lattice parameters of c-GaN [8], [10], [31]. Figure 8 presents the strain profiles taken from RaDMaX simulations (the fits to the experimental data are presented in Figure 7).

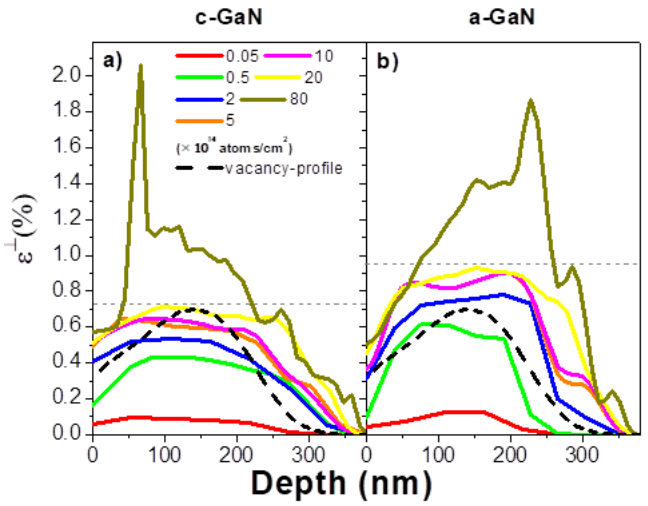

Figure 8 - Strain profiles derived using the RaDMaX code for a) c-GaN and b) a-GaN as a function of depth. The range of 380 nm for the depth axis corresponds to the maximum argon atom range obtained from SRIM simulations. The SRIM vacancy-profile is included for comparison with arbitrary units.

It is clear for both planar orientations that the strain increases with the fluence; in fact, putting aside the highest fluence profile (8 × 10^{15} at/cm^2), the maximum strain value reached for both planar orientations, illustrated by the grey, horizontal, dashed line (~0.7% for c-GaN and ~0.95% for a-GaN) is very similar to the strain value for the implanted volume peak of the second highest fluence (2 × 10^{15} at/cm^2). There is a wide depth region with almost constant strain, which agrees with the fact that the diffractograms show a well-defined second, lower angle peak. A good fit is achieved when using profiles similar to SRIM vacancy-profile for low fluences (up until 1 × 10^{15} at/cm^2), while the transition of the strain profiles from 1 × 10^{15} to 2 × 10^{15} at/cm^2 may indicate a development of the strain around 270 nm, for both planar orientations. As it is possible to observe, the maximum strain is higher for every fluence up until 2 × 10^{15} at/cm^2 for a-GaN than for c-GaN. It has, however, been previously reported that direct comparison between induced strain caused by implantation defects for different planar orientations may not be trivial. Debelle *et al*. [35], [51] pointed out that a two-step model has to be considered when studying induced strain following ion implantation in single crystals.

Further tests with the RaDMaX program showed that it is possible to fit the experimental data well by using quite different strain and DW profiles. Figure 9 presents examples of such different strain profiles for the a-GaN samples implanted with fluences ranging from 5 × 10^{13} at/cm^2 to 2 × 10^{15} at/cm^2, where a region with negative strain (indicating a contraction of the lattice parameter *a*) was considered to better fit the diffractograms at higher angles with respect to the main Bragg peak. This model is, however, dubious as the pronounced shoulder to the right side of the main Bragg peak is already present in the as-grown sample.

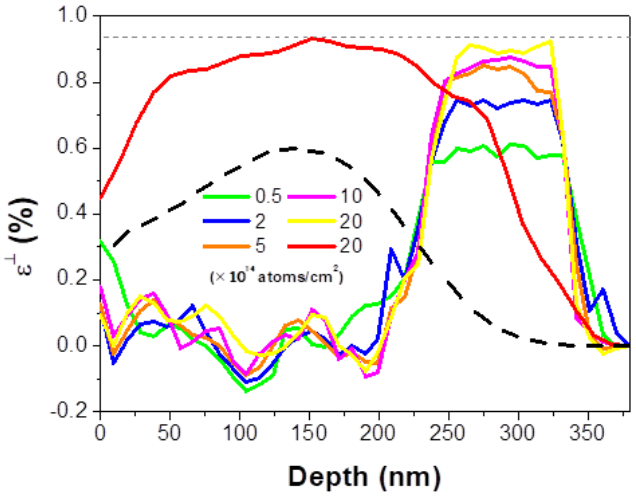

Figure 9 - Alternative RaDMaX strain profiles for the fitting of the diffractograms of five a-GaN samples as a function of depth. The range of 380 nm for the depth axis corresponds to the maximum range of the argon atoms obtained from SRIM simulations. The SRIM vacancy-profile is included with arbitrary units. The red profile has been taken from Figure 8b for comparison.

Important similarities to note in both strain profiles from Figure 8b and Figure 9 are the increase of the strain with the fluence and the wide region where strain is approximately constant. In addition, the maximum strain value reached for all fluences is not only roughly the same for both strain profiles but also in accordance with the experimental data. A crucial difference is, however, the considerable difference in the shape of the profiles in comparison with SRIM simulations, suggesting the bigger unlikelihood of this solution in comparison with the one presented in Figure 8 to describe the induced strain inside the analyzed samples. Regarding the DW factor profiles, very significative differences had been found between the ones corresponding to both strain profiles presented above, which makes it impossible to accurately compare c-plane and a-plane DW factor profiles.

Discussion and Conclusions

The use of complementary RBS/C and XRD techniques made it possible to compare them both, hoping to have a better understanding of the experimental results acquired. While RBS/C is more sensitive to the direct detection of displaced atoms inside the crystalline structure, XRD is sensitive to the distance in-between atomic planes; if there is still diffraction in the presence of defects, hence the complementarity of these techniques.

Figure 10 gives an overview of the main parameters extracted from both techniques, which allows a qualitative comparison of these. It shows the RDL and perpendicular strain as a function of the fluence for both materials orientations. As it has been shown that RaDMaX can accept more than one solution for the same experimental data, the choice for the strain profile here presented was made by taking into consideration the strain profiles which are coherent with SRIM simulations (the ones from Figure 8).

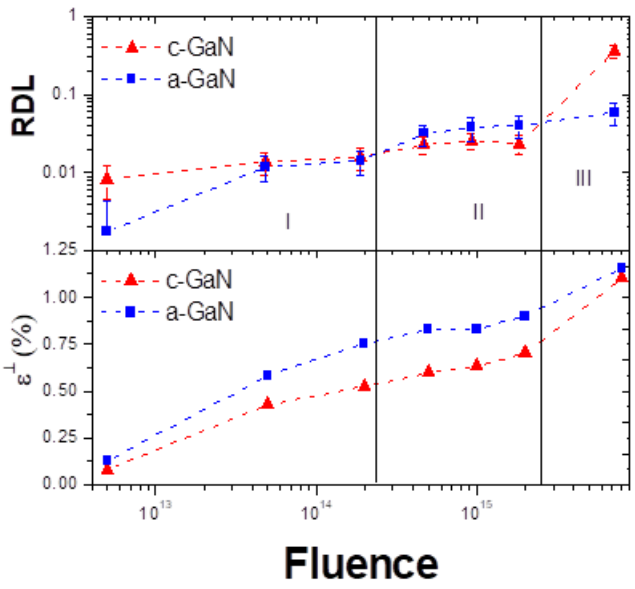

Figure 10 - RDL (relative defect level) and strain values for the depth window and regimes presented in Figure 5 as a function of the fluence.

Even though the RDL for our measurements is below the Hecking curves values at 15 K (Figure 6), our curves seem to follow the shapes of the curves at low temperature. These results are in accordance with the ones presented by Wendler *et al*. [39] and Turos [11]. They have compared damage build-up curves for Ar-implanted c-GaN at different temperatures and presented smaller and shifted values towards higher fluences at room temperature in comparison to implantation at 15 K, indicating not only a recombination of defects at room temperature but also that the transition between regimes occurs at a higher fluence. Both the strain and the relative defect level have been observed to increase with the ion fluence [9]. By relating the three regimes previously to their strain profiles, it is possible to observe a similar development for both planar orientations on the first two regimes: a first one where the increase of the strain is relatively linear as the implanted fluence rises, followed by a second one where the increase is smaller (corresponding to a saturation of the RDL). For the third and last regime of fluence, there is a noticeably higher increase of RDL value observed for c-GaN implanted with 8×10^{15} at/cm^2 than for a-GaN implanted with the same fluence. In the meantime, the strain value for this fluence is nearly the same for both planar orientations. Nevertheless, our XRD data shows similar behavior between the different planar orientations and thus it is not possible to conclude by itself that a-GaN is more resistant to implantation damage than c-GaN for the regime III, which has been previously reported as a consequence of a possible creation of different defect microstructures, following stronger dynamic annealing processes [12], [13].

The main goal of this dissertation was to investigate the strain caused by ion implantation of 300 keV Argon ions in gallium nitride, for two planar orientations (a-plane and c-plane) and compare the strain evolution with the number of displaced atoms. The ultimate proof to confirm that strain as the driving force of damage

accumulation, was not possible to deliver within the restricted time frame of this thesis. Possible future work to contribute to clarifying the validity of this hypothesis include the study of damage and strain build-up following implantation at different temperatures. This would provide the possibility to study whether the transition between damage build-up regimes takes place, for different implantation temperatures, at the same strain value. Practical applications of this study include the development of electronics based on GaN, which is among the most popular wide band gap materials currently under research.

5. References

[1] S. Nakamura and S. F. Chichibu, *Introduction to Nitride Semiconductor Blue Lasers and Light Emitting Diodes*. Boca Raton, FL: CRC Press, 2000.

[2] F. A. Ponce and D. P. Bour, "Nitride based semiconductors for blue and green light-emitting devices," *Nature*, vol. 386, pp. 351–359, 1997.

[3] A. Lidow, J. Strydom, M. de Rooij, and D. Reusch, *GaN Transistors for Efficient Power Conversion*, 2nd Editio. Hoboken, NJ: Wiley, 2014.

[4] M. A. Nastasi and J. W. Mayer, *Ion Implantation and Synthesis of Materials*. Berlin Heidelberg: Springer, 2006.

[5] J. I. Pankove and J. A. Hutchby, "Photoluminescence of Zn-implanted GaN," *Appl. Phys. Lett.*, vol. 24, no. 6, pp. 281–283, 1974.

[6] H. H. Tan *et al.*, "Annealing of ion implanted gallium nitride," *Appl. Phys. Lett.*, vol. 72, no. 10, pp. 1190–1192, 1998.

[7] E. V Kalinina, A. S. Zubrilov, A. M. Strel'chuk, V. A. Solov'ev, and V. A. Dmitriev, "Electrical and optical properties of Mg ion implanted GaN p-n junctions," in *HITEN 99. Third European Conference on High Temperature Electronics*, 1999, pp. 91–94.

[8] S. O. Kucheyev, J. S. Williams, and S. J. Pearton, "Ion implantation into GaN," *Mater. Sci. Eng. R Reports*, vol. 33, no. 2–3, pp. 51–107, 2001.

[9] B. Pipeleers, S. M. Hogg, and A. Vantomme, "Defect accumulation during channeled erbium implantation into GaN," *J. Appl. Phys.*, vol. 98, no. 12, 2005.

[10] F. Gloux, T. Wojtowicz, P. Ruterana, K. Lorenz, and E. Alves, "Transmission electron microscopy investigation of the structural damage formed in GaN by medium range energy rare earth ion implantation," *J. Appl. Phys.*, vol. 100, no. 7, 2006.

[11] A. Turos, "On the mechanism of damage build-up in GaN," *Radiat. Eff. Defects Solids*, vol. 168, no. 6, pp. 431–441, 2013.

[12] K. Lorenz *et al.*, "Implantation damage formation in a-, c- and m-plane GaN," *Acta Mater.*, vol. 123, pp. 177–187, 2017.

[13] N. Catarino *et al.*, "Enhanced dynamic annealing and optical activation of Eu implanted a-plane GaN," *Epl*, vol. 97, no. 6, 2012.

[14] K. Pągowska *et al.*, "RBS/channeling and TEM study of damage buildup in ion bombarded GaN," *Acta Phys. Pol. A*, vol. 120, no. 1, pp. 153–155, 2011.

[15] T. Paskova, *Nitrides with Nonpolar Surfaces*. Weinheim: Wiley-VCH, 2008.

[16] Y. Taniyasu and M. Kasu, "Improved emission efficiency of 210-nm deep-ultraviolet aluminum nitride light-emitting diode," *NTT Tech. Rev.*, vol. 8, no. 8, 2010.

[17] T. Detchprohm, K. Hiramatsu, K. Itoh, and I. Akasaki, "Relaxation Process of the Thermal Strain in the Gan/Alpha-Al2O3 Heterostructure and Determination of the Intrinsic Lattice-Constants of Gan Free From the Strain," *Japanese J. Appl. Phys. Part 2-Letters*, vol. 31, pp. L1454–L1456, 1992.

[18] M. Leszczynski *et al.*, "Lattice parameters of gallium nitride," *Appl. Phys. Lett.*, vol. 69, no. 1, pp. 73–75, 1996.

[19] B. Gil, *Physics of Wurtzite Nitrides and Oxides*. Cham: Springer, 2014.

[20] M. Grundmann, *The Physics of Semiconductors: An Introduction Including Nanophysics and Applications*, 2nd ed. Berlin: Springer-Verlag Berlin and Heidelberg GmbH & Co. KG, 2010.

[21] J. Zou, D. Kotchetkov, A. A. Balandin, D. I. Florescu, and F. H. Pollak, "Thermal conductivity of GaN films: Effects of impurities and dislocations," *J. Appl. Phys.*, vol. 92, no. 5, pp. 2534–2539, 2002.

[22] H. Amano, N. Sawaki, I. Akasaki, and Y. Toyoda, "Metalorganic vapor phase epitaxial growth of a high quality GaN film using an AlN buffer layer," *Appl. Phys. Lett.*, vol. 48, no. 5, pp. 353–355, 1986.

[23] J. Jasinski, D. N. Zakharov, and L. Berkeley, "GaN grown in polar and non-polar directions," *Opto-Electronics Rev.*, vol. 12, no. 4, pp. 339–346, 2004.

[24] A. Chakraborty, K. C. Kim, F. Wu, J. S. Speck, S. P. DenBaars, and U. K. Mishra, "Defect reduction in nonpolar a-plane GaN films using in situ SiN_x nanomask," *Appl. Phys. Lett.*, vol. 89, no. May 2014, p. 41903, 2006.

[25] J. Hertkorn *et al.*, "Optimization of nucleation and buffer layer growth for improved GaN quality," *J. Cryst. Growth*, vol. 308, no. 1, pp. 30–36, 2007.

[26] J. Hertkorn *et al.*, "Process optimization for the effective reduction of threading dislocations in MOVPE grown GaN using in situ deposited SiN_x masks," *J. Cryst. Growth*, vol. 310, no. 23, pp. 4867–4870, 2008.

[27] F. Bernardini and V. Fiorentini, “Macroscopic polarization and band offsets at nitride heterojunctions,” *Phys. Rev. B - Condens. Matter Mater. Phys.*, vol. 57, no. 16, pp. R9427–R9430, 1998.

[28] P. Waltereit *et al.*, “Nirtride semiconductors free of electrostatic fields for efficient white light-emitting diodes,” *Nature*, vol. 406, no. 6798, pp. 865–868, 2000.

[29] S. O. Kucheyev, J. S. Williams, J. Zou, and C. Jagadish, “Dynamic annealing in III-nitrides under ion bombardment,” *J. Appl. Phys.*, vol. 95, no. 6, pp. 3048–3054, 2003.

[30] E. Wendler, A. Kamarou, E. Alves, K. Gärtner, and W. Wesch, “Three-step amorphisation process in ion-implanted GaN at 15 K,” *Nucl. Instruments Methods Phys. Res. Sect. B Beam Interact. with Mater. Atoms*, vol. 206, pp. 1028–1032, 2003.

[31] B. Lacroix, S. Leclerc, A. Declémy, K. Lorenz, E. Alves, and P. Ruterana, “Mechanisms of damage formation in Eu-implanted GaN probed by X-ray diffraction,” *J. Appl. Phys.*, vol. 112, no. 7, 2011.

[32] C. Liu, B. Mensching, K. Volz, and B. Rauschenbach, “Lattice expansion of Ca and Ar ion implanted GaN,” *Appl. Phys. Lett.*, vol. 71, no. 16, pp. 2313–2315, 1997.

[33] D. N. Faye *et al.*, “Mechanisms of Implantation Damage Formation in $Al_xGa_{1-x}N$ Compounds,” *J. Phys. Chem. C*, vol. 120, no. 13, pp. 7277–7283, 2016.

[34] S. Magalhães, M. Fialho, M. Peres, K. Lorenz, and E. Alves, “Quantitative x-ray diffraction analysis of bimodal damage distributions in Tm implanted $Al_{0.15}Ga_{0.85}N$,” *J. Phys. D. Appl. Phys.*, vol. 49, no. 13, p. 135308, 2016.

[35] A. Debelle and A. Declémy, “XRD investigation of the strain/stress state of ion-irradiated crystals,” *Nucl. Instruments Methods Phys. Res. Sect. B Beam Interact. with Mater. Atoms*, vol. 268, no. 9, pp. 1460–1465, 2010.

[36] M. Souilah, A. Boulle, and A. Debelle, “RaDMaX: A graphical program for the determination of strain and damage profiles in irradiated crystals,” *J. Appl. Crystallogr.*, vol. 49, pp. 311–316, 2016.

[37] A. Turos, P. Jóźwik, M. Wójcik, J. Gaca, R. Ratajczak, and A. Stonert, “Mechanism of damage buildup in ion bombarded ZnO,” *Acta Mater.*, vol. 134, pp. 249–256, 2017.

[38] A. Debelle *et al.*, “Lattice strain in irradiated materials unveils a prevalent defect evolution mechanism,” *Phys. Rev. Mater.*, vol. 2, no. 1, p. 13604, 2018.

[39] E. Wendler *et al.*, “Comparison of low-and room-temperature damage formation in Ar ion implanted GaN and ZnO,” *Nucl. Instruments Methods Phys. Res. Sect. B Beam Interact. with Mater. Atoms*, vol. 307, pp. 394–398, 2013.

[40] F. Scholz, P. Brückner, F. Habel, M. Peter, and K. Köhler, “Improved GaN layer morphology by hydride vapor phase epitaxy on misoriented Al_2O_3 wafers,” *Appl. Phys. Lett.*, vol. 87, no. 18, pp. 1–3, 2005.

[41] S. Schwaiger, F. Lipski, T. Wunderer, and F. Scholz, “Influence of slight misorientations of r-plane sapphire substrates on the growth of nonpolar a-plane GaN layers via HVPE,” *Phys. Status Solidi C*, vol. 7, no. 7–8, pp. 2069–2072, 2010.

[42] J. F. Ziegler, M. D. Ziegler, and J. P. Biersack, “SRIM - The Stopping and Range of Ions in Matter,” *Nucl. Instr. Meth. B*, vol. 268, pp. 1818–1823, 2010.

[43] W.-K. Chu, J. W. Mayer, and M.-A. Nicolet, *Backscattering Spectrometry*. Orlando: Academic Press, 1978.

[44] G. Schatz and A. Weidinger, *Nuclear Condensed Matter Physics: Nuclear Methods and Applications*. Chichester: Wiley, 1996.

[45] K. Gärtner, “Modified master equation approach of axial dechanneling in perfect compound crystals,” *Nucl. Instruments Methods Phys. Res. Sect. B Beam Interact. with Mater. Atoms*, vol. 227, no. 4, pp. 522–530, 2005.

[46] E. Wendler, W. Wesch, and G. Götz, “Radiation damage and optical properties of Ar+-implanted GaP,” *J. Appl. Phys.*, vol. 70, no. 1, pp. 144–149, 1991.

[47] M. Hrabak, R. S. Padovan, M. Kralik, D. Ozretic, and K. Potocki, “Nikola Tesla and the Discovery of X-rays,” *RadioGraphics*, vol. 28, no. 4, pp. 1189–1192, 2008.

[48] E. T. Yu and M. O. Manasreh, *III-V Nitride Semiconductors: Applications and Devices*. New Work: Taylor & Francis, 2003.

[49] Y. Zhang *et al.*, “Damage profile and ion distribution of slow heavy ions in compounds,” *J. Appl. Phys.*, vol. 105, no. 10, 2009.

[50] N. Hecking, K. F. Heidemann, and E. Te Kaat, “Model of temperature dependent defect interaction and amorphization in crystalline silicon during ion irradiation,” *Nucl. Inst. Methods Phys. Res. B*, vol. 15, no. 1–6, pp. 760–764, 1986.

[51] A. Debelle *et al.*, “Influence of elastic properties on the strain induced by ion irradiation in crystalline materials,” *J. Phys. D. Appl. Phys.*, vol. 46, no. 4, 2013.